29th AIAA Applied Aerodynamics Conference
27 - 30 June 2011, Honolulu, Hawaii

AIAA 2011-3796

Experimental Investigation of a Large-Scale Low-Boom Inlet Concept

Stefanie M. Hirt,[1] Rodrick V. Chima,[2] and Manan A. Vyas[3]
NASA Glenn Research Center, Cleveland, OH, 44135

Thomas R. Wayman[4] and Timothy R. Conners[5]
Gulfstream Aerospace Corporation, Savannah, GA, 31402

and

Robert W. Reger[6]
University of Florida, Gainesville, FL, 32603

A large-scale low-boom inlet concept was tested in the NASA Glenn Research Center 8- x 6- foot Supersonic Wind Tunnel. The purpose of this test was to assess inlet performance, stability and operability at various Mach numbers and angles of attack. During this effort, two models were tested: a dual stream inlet designed to mimic potential aircraft flight hardware integrating a high-flow bypass stream; and a single stream inlet designed to study a configuration with a zero-degree external cowl angle and to permit surface visualization of the vortex generator flow on the internal centerbody surface. During the course of the test, the low-boom inlet concept was demonstrated to have high recovery, excellent buzz margin, and high operability. This paper will provide an overview of the setup, show a brief comparison of the dual stream and single stream inlet results, and examine the dual stream inlet characteristics.

Nomenclature

AOA	=	inlet angle of attack
c_x	=	vortex generator axial chord length
DC60	=	distortion descriptor, $((p_{t,av}-p_{t,60min})/p_{t,av})$
DPCP	=	average ARP1420 circumferential distortion
h	=	vortex generator height
N	=	number of vortex generator devices
$p_{t,av}$	=	average AIP total pressure
$p_{t,60min}$	=	average total pressure for the 60° sector at the AIP with the lowest total pressure
s	=	vortex generator spacing

I. Introduction

A. Background

HIGH inlet efficiency, low flow spillage, and highly streamlined nacelle surfaces are all important characteristics for inlets designed for supersonic aircraft with low sonic boom signatures. Many inlet designs for legacy

[1] Aerospace Engineer, Inlets and Nozzles Branch, MS 5-12, Senior Member AIAA.
[2] Aerospace Engineer, Inlets and Nozzles Branch, MS 5-12, Associate Fellow AIAA.
[3] Aerospace Engineer, Inlets and Nozzles Branch, MS 5-12, Member AIAA.
[4] Technical Specialist–Applied Aerodynamics, Preliminary Design Department, M/S R-07, Associate Fellow AIAA.
[5] Principal Engineer–Propulsion, Preliminary Design Department, M/S R-07, Associate Fellow AIAA.
[6] Undergraduate Student Research Program Researcher, Member AIAA.

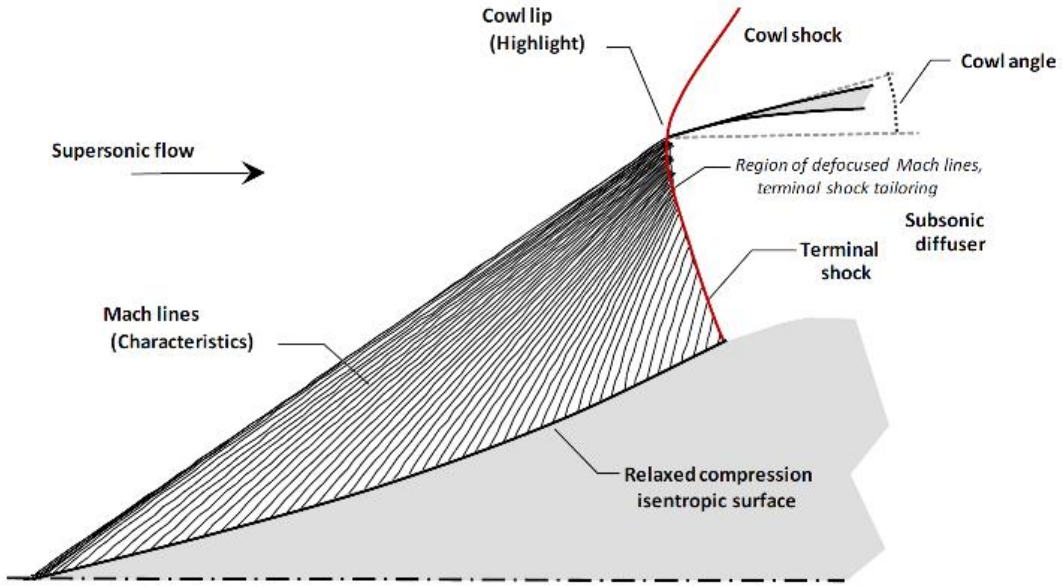

Figure 1. Relaxed external compression inlet showing shock tailoring to reduce the required cowl lip angle.

supersonic aircraft incorporated complex mechanical systems, such as variable geometry and boundary layer bleed systems, to improve total pressure recovery and, hence, engine performance. But none are known to incorporate features that directly address the sonic boom problem.

Gulfstream Aerospace has developed a novel inlet design which improves supersonic performance while decreasing inlet complexity[1] and the inlet's contribution to the overall sonic boom signature of the aircraft. The design incorporates a fixed-geometry external isentropic compression surface which relaxes the compression region at the cowl lip,[2] as shown in Fig 1. In doing so, the cowl angle, the propulsion system drag, and the strength of the sonic boom created by the nacelle are reduced[3]. In addition, the Gulfstream inlet concept incorporates a large secondary bypass system that permits a more streamlined nacelle by eliminating the bulge in the cowling traditionally associated with the engine accessory gearbox[4]. The bypass system also reduces spillage by improving inlet-engine matching, especially at off-design operating conditions. The reduced spillage and improved nacelle shaping further attenuate the propulsion system's contribution to sonic boom.

While high in performance, the relaxed compression design technique has two primary drawbacks, as discussed by Conners[5] *et al*. The first is increased tip radial distortion caused by a stronger compression field gradient due to relaxed compression. However, the impact of this can be minimized by vigilant fan blade and subsonic flow path design. The second challenge is the thick boundary layer that develops on the centerbody aft of the terminal shock due to the increased turning angle required to maintain the desired diffusion profile. In this case, flow control can be required to improve the uniformity of the pressure profile ingested into the compressor.

Many supersonic inlets rely on bleed to improve engine efficiency and stability by reducing flow blockage and the tendency for flow to separate from the diffuser walls. However, bleeding leads to increased mechanical complexity, thereby decreasing mechanical robustness and increasing cost. Drag associated with bleed also has an adverse impact on vehicle performance. Passive control devices, such as arrays of vortex generators (VGs), are one approach to improving boundary layer health in such a way that reduces or eliminates the need for the increased mechanical complexity associated with bleed-based systems[6].

In addition, the high-flow nacelle bypass concept represents a new design technique that had little empirical data available to substantiate it prior to testing in the 8-by-6 ft supersonic wind tunnel. A major area of uncertainty associated with the concept included its ability to successfully pass a large fraction of captured inlet flow around the engine with minimal losses and with no adverse dynamics.

B. Test Objectives

The general purpose of this test was to evaluate a large-scale low-boom supersonic inlet concept using the NASA 8- by 6- foot Supersonic Wind Tunnel. Specific objectives were: 1) to experimentally investigate the feasibility of using a high-flow nacelle bypass in a supersonic inlet design; 2) to determine if zero-spillage is a feasible target for a

simple relaxed external compression system coupled with high-flow bypass; 3) to investigate the practicality of an ultra-low angle cowl configuration enabled by relaxed external compression; 4) to assess the dynamic characteristics of a coupled bypass/primary inlet system[7]; 5) to evaluate the influence of vortex generators on shock stability; 6) to evaluate simple, bleedless VG-based inlet boundary layer control options; and 7) to obtain data for CFD code validation.

Test data were acquired to assess inlet performance, stability, and operability at various flow rates, supersonic Mach numbers, and angles of attack. Two models were tested: a dual stream inlet designed to mimic potential aircraft flight hardware integrating a high-flow bypass stream; and a single stream inlet designed to study a configuration with a zero-degree external cowl angle and to permit surface visualization of the vortex generator flow on the internal centerbody surface. Each inlet was tested with a series of VG configurations to determine the usefulness of these simple, passive devices in controlling boundary layer health and maintaining normal shockwave stability. This paper will provide an overview of the setup, show a brief comparison of the dual stream and single stream inlet results, explain the dual stream inlet characteristics, and discuss several overall conclusions.

II. Test Setup and Apparatus

A. Tunnel Setup and Test Conditions

All testing was carried out in the 8- x 6- foot Supersonic Wind Tunnel[8] (8x6 SWT) located at NASA Glenn Research Center. The 8x6 SWT is an atmospheric tunnel capable of test section Mach numbers from 0.36 to 2.0. For this test, the tunnel was run in the aerodynamic cycle with the model in the porous wall transonic test section mounted on the supersonic strut. The strut was actuated to control the model angle of attack (AOA), and the strut height was varied for each AOA to maintain the inlet tip on the centerline of the 26.5 in diameter schlieren window.

The inlet was tested over a range of Mach numbers from 0.5 to 1.8, and at AOAs from -2˚ to +5˚. The actual tunnel Mach number was slightly less than nominal to allow repeatable and stable conditions. Blockage limits prevented the inlet from being tested over the entire AOA range for lower supersonic Mach numbers. Table 1 shows the combinations of Mach number and AOA that were tested. A cold pipe and mass flow plug were used to throttle and measure the flow through the inlet.

Table 1. Tunnel configuration test matrix showing Mach numbers and their corresponding angle of attack

Mach Number		Angles of Attack						
nominal	actual							
1.8	1.78	-2.0˚	-1.0˚	0.0˚	1.0˚	2.0˚	3.0˚	5.0˚
1.7	1.67	-2.0˚	-1.0˚	0.0˚	1.0˚	2.0˚	3.0˚	5.0˚
1.6	1.56	-2.0˚	-1.0˚	0.0˚	1.0˚	2.0˚	3.0˚	
1.5	1.45	-1.0˚	0.0˚	1.0˚				
1.4	1.35	0.0˚						
0.5	0.51	-2.0˚	-1.0˚	0.0˚	1.0˚	2.0˚	3.0˚	5.0˚

B. Inlet Configurations

As part of this large-scale low-boom inlet test, two complementary inlet configurations were tested. The two inlets were designed for a vehicle flying at Mach 1.6 with Mach 1.7 overwing. Both the dual stream and single stream inlets had the same centerbody contour, shown as the blue curve in Fig. 2, which created a relaxed isentropic compression leading to a normal shock Mach number of approximately 1.3 near the centerbody surface and about 1.6 in the cowl region. Also noted in Fig. 2 are the axial locations of the upstream and downstream vortex generators, the forward and aft boundary layer rakes, and the 0˚ top-dead-center line static taps. The static taps are shown on a static pressure profile near peak inlet recovery from an early CFD solution that was used to help determine the static tap locations.

The inlets also had the same 12 in inlet diameter at the cowl lip. For both models, x = 0 in was defined as the theoretical centerbody sharp tip location. Due to a spike tip radius of 0.005 in, the x-location of the physical spike tip was x = 0.035 in. For both inlets, the cowl lip was located at an axial station of 8.10 in, with a cowl lip radius of 0.01 in. The aerodynamic interface plane (AIP) was located at an axial station of x = 26.05 in.

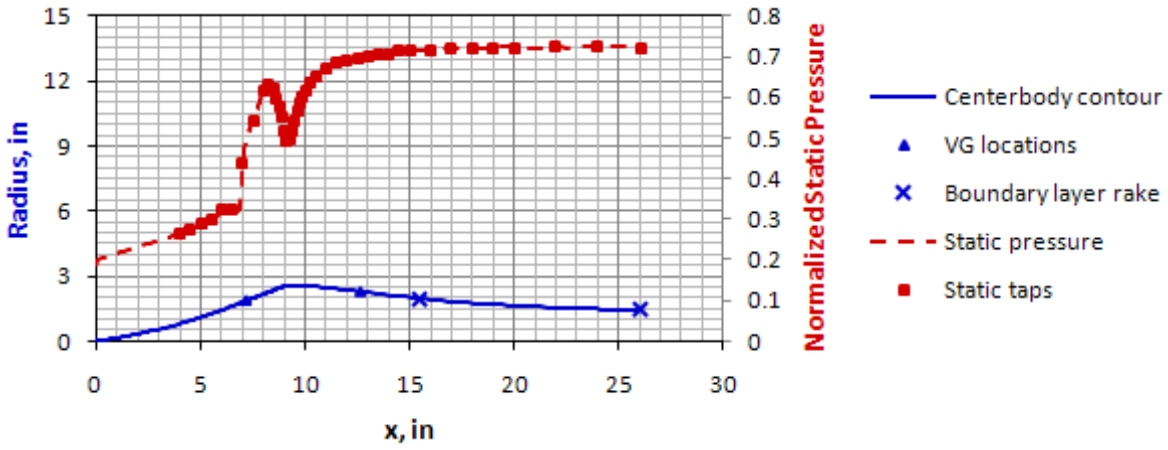

Figure 2. Centerbody contour and instrumentation locations

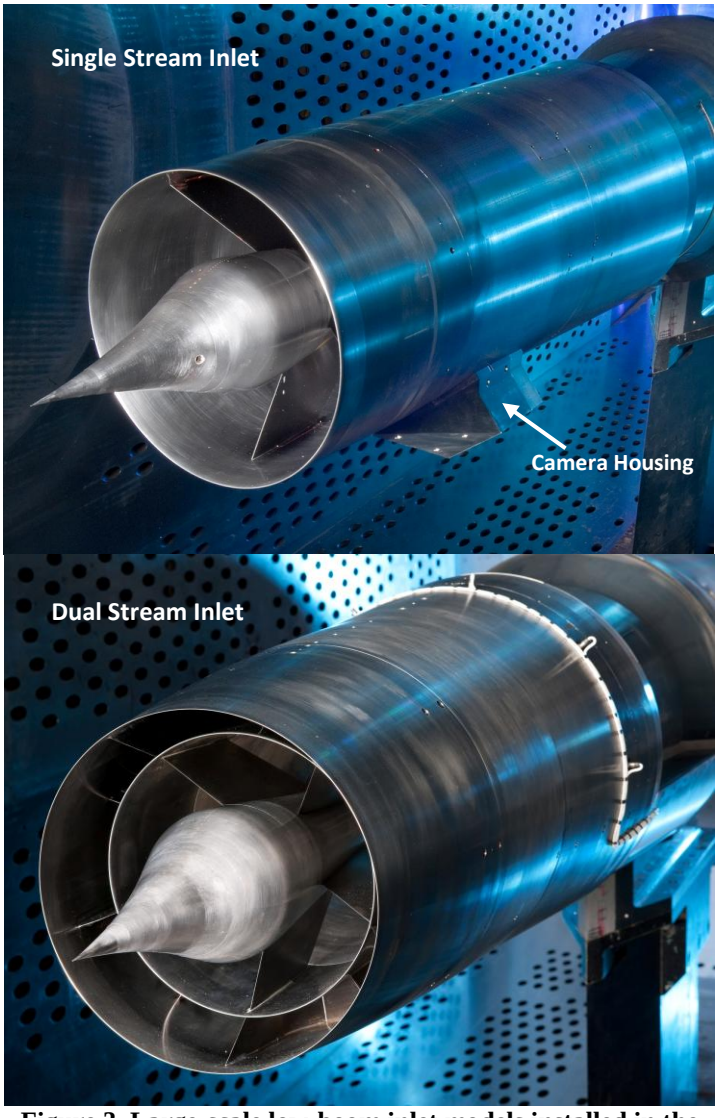

Figure 3. Large-scale low-boom inlet models installed in the 8x6-ft tunnel.

The single stream inlet, shown in Figs. 3 and 4, had a zero-degree exterior cowl angle. All the captured flow exited through the 16 in diameter cold pipe and mass flow plug. A diffuser was used to transition from the 11.75 in diameter at the AIP to the larger cold pipe diameter to obtain approximately Mach 0.3 in the cold pipe. The single stream inlet incorporated a camera housing on the cowl to observe surface flow visualization on the internal centerbody surfaces during testing.

The dual stream inlet, shown in Figs. 3 and 4, was separated into two channels. The inner primary channel, or core as labeled in Fig. 4, fed into the 16 in diameter mass flow plug. The outer bypass channels were controlled by exit plates with annular slots with a fixed exit area that would provide the desired bypass ratio. Four exit plate areas (1.0, 1.1, 1.2 and 1.3) were tested to determine the appropriate exit condition. The 1.0 exit plate had a flow area equal to the theoretical area required to provide the design flow split based on one-dimensional flow analysis. Initial testing determined that the exit plate with an area equal to 1.2 times the theoretical area most closely matched the desired flow split, which for this test was a bypass to core flow ratio of 0.7. The bypass flow path started as a 360-degree annulus, but was compressed to 200 degrees over the first 17.87 in of the duct. At flight scale, this would accommodate the engine gearbox. For a low boom design, it was preferred to enclose the gearbox within the nacelle. The bypass flow was divided into five equal area channels with an additional

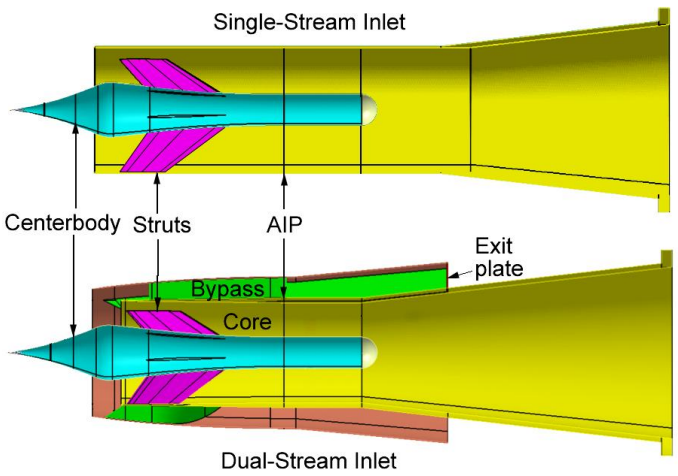

Figure 4. Single Stream and Dual Stream inlet comparison.

vane in the center of each channel to help guide the flow around the gearbox fairing.

The single stream inlet and the core path of the dual stream inlet had five primary struts in the subsonic diffuser. Five was preferred because it was undesirable to present the engine with a multiple of two or three per rev pattern. Both core paths also had a set of three secondary struts downstream of the AIP (not shown in Fig. 4). These struts provided additional structural stability for the model as well as providing space to route instrumentation out of the centerbody.

C. Instrumentation and Data Systems

Data for this test were acquired using steady state and high frequency response pressure measurements as well as several flow visualization techniques. The steady state pressures were measured with Pressure Systems, Inc. ESP pressure scanners and stored by the Escort D+ data system. Data was sampled once per second, and 5 samples were averaged for each recording. The steady state pressure measurement system had an uncertainty of ±0.02 psi.

The single stream model had 127 static pressure taps. Ninety static pressure taps were placed on the centerbody with 41 on the 0˚ top-dead-center line. Figure 2 shows the spacing of the static taps on the 0˚ line laid on a pressure contour from an early computational fluid dynamics solution. The remaining centerbody taps were distributed as follows: 21 static taps on the 90˚ line, 20 static taps at the midpoint between the struts in 5 axial planes, and 8 static taps spaced circumferentially at the AIP. The inner cowl surface was instrumented with 17 static pressure taps. In the diffuser and cold pipe there were 5 rings of 4 static pressure taps each. The statics taps at the midpoint of the cold pipe were used for the mass flow calculations, and the last ring on the aft face of the cold pipe was used to measure base pressure and confirm that the plug was choked.

The static pressure instrumentation on the dual steam model was the same as the single stream with two exceptions. The 17 inner cowl surface taps from the single stream were located on the inner surface of the bypass splitter for the dual stream inlet. Also, 5 additional statics were added: one in each of the bypass channels.

Total pressure measurements for both inlets were made with an array of pitot rakes. The AIP was instrumented with 8 rakes to measure total pressure recovery and steady state distortion. The rakes at 0˚, 90˚, 180˚, and 270˚ each had 5 steady state and 1 high frequency response probes. The steady state probes were arrayed at the centers of equal area sections, as in ARP 1420[9]. The high response probe was halfway between the centerbody surface and the nearest steady state probe on an area basis. The rakes at 45˚, 135˚, 225˚, and 315˚ each had 6 steady state and 1 high frequency response probes. Five of the steady state probes were arrayed at the centers of equal area sections, as in ARP 1420, and the sixth was halfway between the centerbody surface and the nearest probe on an area basis. The high frequency response probe was on the cowl/splitter side, halfway between the two outermost probes on an area basis. Inlet total pressure recoveries reported in this paper are calculated using only the 40 steady state probes as defined in ARP 1420.

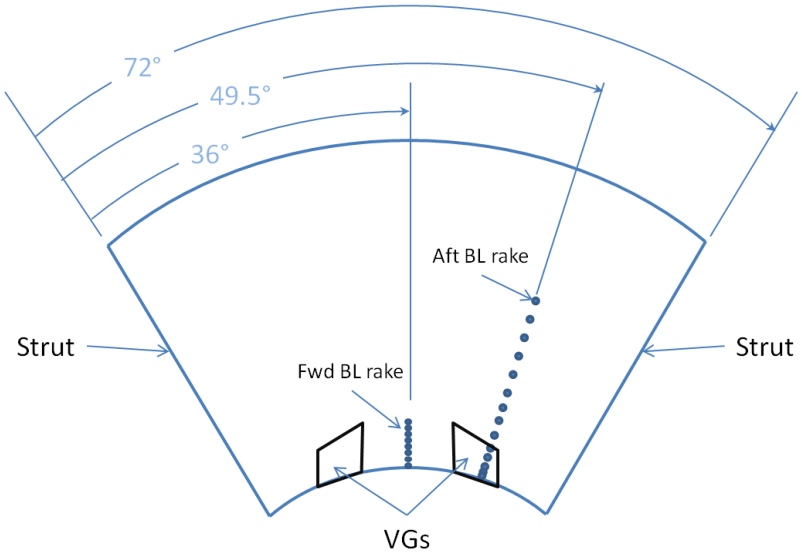

Figure 5. Location of boundary layer rakes relative to VGs.

Two boundary layer rakes were included to help characterize the

effects of the vortex generators on the centerbody boundary layer. The upstream boundary layer rake was an 8 probe rake at an axial station of x = 15.5 in and a circumferential position of 144˚. The downstream rake had 14 probes and was located at the AIP at a circumferential position of 202.5˚. The position of the rakes relative to the primary struts and VGs is shown in Fig. 5. The dual stream inlet also had one 5 probe rake in the center of each of the 5 bypass channels at an axial station of 35.0 in. The bypass rakes were used to calculate the mass flow and recovery in the bypass.

The high frequency response pressures were measured with Kulite transducers and recorded at 5 kHz by the Dewetron data system. The single stream inlet had 20 high frequency response pressure measurements with 8 on the centerbody surface, 8 in the AIP rake array, and 4 in the cold pipe. The dual stream inlet model had 9 additional high frequency response pressure measurements: one in each of the 5 bypass channels, and 4 in the diffuser.

In addition to the traditional pressure instrumentation, four flow visualization techniques were used to provide additional insight. The facility schlieren system was used with a Phantom V310 high speed camera recoding at 2000 and 4200 frames per second to capture low amplitude dynamics near the design point and buzz cycles. The inlet spike and cowl lip were in view for all angles of attack. Still images were captured for a subset of the steady operating points.

Boundary layer transition was confirmed using a chemical sublimation technique. A mixture of fluorene ($C_{13}H_{10}$) and a solvent (Flux Remover C) were applied to the inlet spike using a commercial aerosol paint gun. Precautions were taken for personnel safety and to prevent migration of the material into the static pressure ports or the dynamic pressure transducers. Appearing on the model as white powder coating, the fluorene sublimes at a rate faster in regions of greater heat-transfer coefficients. This is typically the case for turbulent boundary layers as compared with laminar boundary layers, except in the region of stagnation points like wing leading edges. The sublimation process showed that natural boundary layer transition was occurring upstream of the intended boundary layer trip grit placement on the model, and so the test was conducted without any boundary layer trip.

Two flow visualization techniques, pressure sensitive paint and oil flow visualization, were used on both external and internal inlet surfaces on the single stream inlet. The external inlet spike and cowl surfaces were viewed through the schlieren windows in the tunnel wall. The internal centerbody surface was imaged with a camera viewing through an opening in the cowl surface. The camera housing containing the CMOS camera, LEDs, and a water cooling system can be seen attached to the lower side of the single stream inlet in Fig. 3.

D. Vortex Generators

The inlet model incorporated replaceable rings of vortex generators (VGs) at two axial stations on the centerbody. The positions of the VGs in the inlet are indicated by the blue triangles in Fig. 2. The upstream vortex generator ring was located on the compression surface forward of the normal shock, with the trailing edge of the devices at x = 7.15 in. The upstream VGs were designed to help mitigate any separation or normal shock unsteadiness due to the normal shock wave-boundary layer interaction, or the amount of turning at the shoulder. The downstream VG ring was in the subsonic diffuser just ahead of the primary struts, with the trailing edge of the devices at x = 12.605 in. The downstream VGs were designed to improve the flow distribution at the AIP.

Table 2. Upstream and downstream vortex generator definitions.

Type	Designation	*s*, in	*h*, in	c_x, in	N[1]
Microramp	U1	0.549	0.075	0.308	20
Microramp	U2	0.283	0.038	0.156	40
Split ramp	U3	0.733	0.075	0.308	15
Split ramp	U4	0.377	0.038	0.156	30
Vane[2]	D1	1.181	0.400	0.961	10 (5)
Vane[3]	D2	1.181	0.400	0.961	10 (5)
Plough	D3	3.104	0.400	0.961	5
Ramp	D4	3.054	0.400	0.961	5
Vane[3]	D5	0.565	0.250	0.600	20 (10)
Ramp	D6	3.054	0.250	0.600	10

[1] Number of devices (Vane pairs)
[2] Vanes arrayed as upwash pairs
[3] Vanes arrayed as downwash pairs

Four upstream and six downstream VG configurations were tested. The upstream VGs consisted of microramp and split ramp configurations, each in two sizes. For the downstream VGs, the larger devices were laid out with one vortex pair (a single ramp or plow, or two vanes) in each of the five

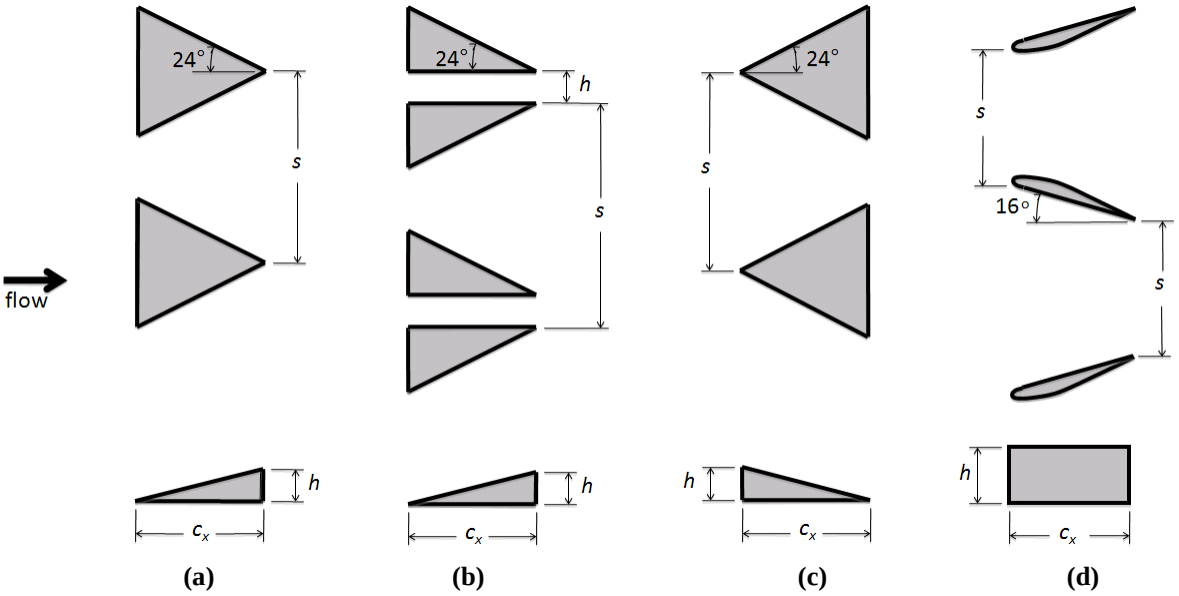

Figure 6. Vortex generator configurations showing the top and side view for (a)microramp/ramp style, (b) split ramp style, (c) plow style, and (d) vane style devices.

passages between the primary struts. The smaller devices were laid out with two vortex pairs in each passage. Each style of vortex generators tested is shown with key dimensions defined in Fig. 6. Throughout the paper, the configurations are referred to by the designations listed in Table 2, with U0D1 representing no upstream VGs and the D1 downstream VG configuration.

E. Computational Fluid Dynamics

Computational fluid dynamics (CFD) results were instrumental to the success of this test. Figure 7 shows sample results from calculations that were made with several different CFD codes to plan different parts of the test; they include the following.

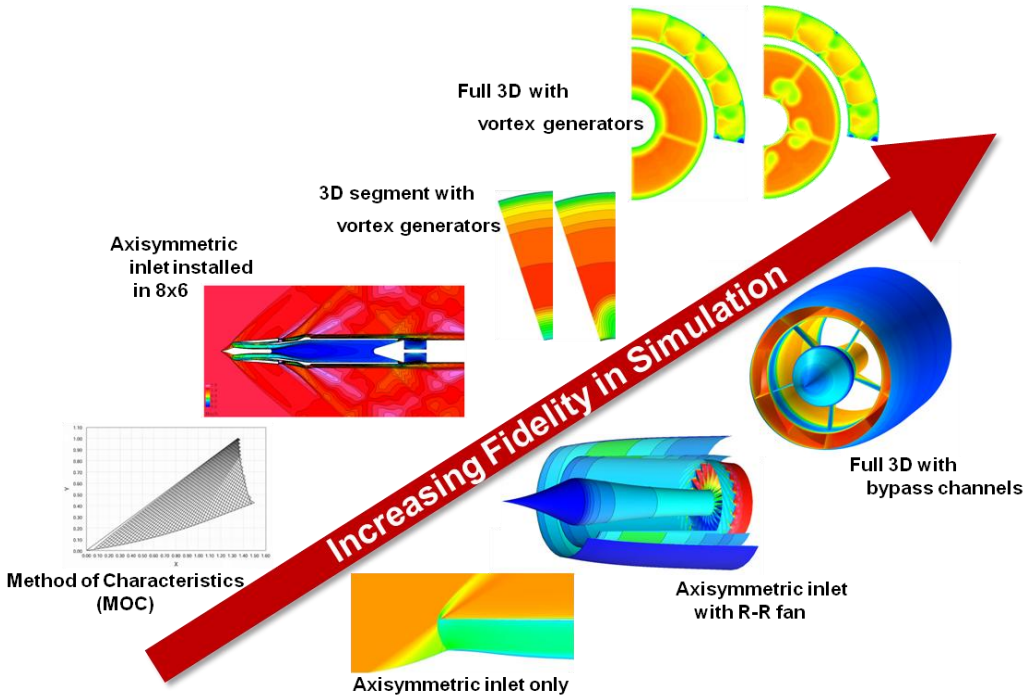

Figure 7. Computational fluid dynamics analyses contributing to the inlet test.

- The compression spike was designed using a method of characteristics code[10].
- Axisymmetric analyses were done to refine the design, predict general performance trends, and size the bypass exit plates[11].
- An analysis of the dual-stream inlet coupled to a Rolls-Royce fan was done to predict engine stability characteristics[12].
- 3-D analyses of the dual-stream inlet including struts and bypass geometry were performed to investigate effects of the curved bypass vanes and angle of attack[13,14].
- The inlets were analyzed with microramps and vane vortex generators to determine optimal sizes and placements of the flow control devices[14-16].

III. Results

A. Dual Stream and Single Stream Inlet Comparisons

Overall inlet performance is described by the inlet cane curve, which shows the variation in total pressure recovery as a function of mass flow ratio, and AIP distortion levels. Total pressure recovery is defined as the average total pressure measured at the AIP divided by the freestream total pressure. The mass flow ratio is defined as the total mass flow captured by the inlet, including both the core and bypass stream flow for the dual stream inlet, divided by the capture mass flow rate.

The cane curves for the dual and single stream inlets are shown in Fig. 8 for Mach 1.7, 0˚ AOA. Because the tunnel operated at Mach 1.67 rather than the inlet design point of 1.7, the maximum mass flow ratio was 0.985 for the dual stream inlet and 0.978 for the single stream inlet.

Inlet recoveries are often compared to military specification MIL-E-5008B expected recovery values, which is 0.956 at Mach 1.67. The single stream inlet peak recovery was 0.947 at a mass flow ratio of 0.964. The lower pressure recovery in the single stream inlet was due to the shock losses on the cowl side, where the normal shock Mach number was approximately 1.6. The dual stream inlet had a peak recovery of 0.965 at the AIP for a mass flow ratio of 0.969. The dual stream recovery is higher because the bypass channel diverted the high loss flow near the cowl around the engine. The recovery through the bypass channel is shown in Fig. 9. At the mass flow ratio where the inlet reached peak recovery, the bypass channel recovery was 0.864.

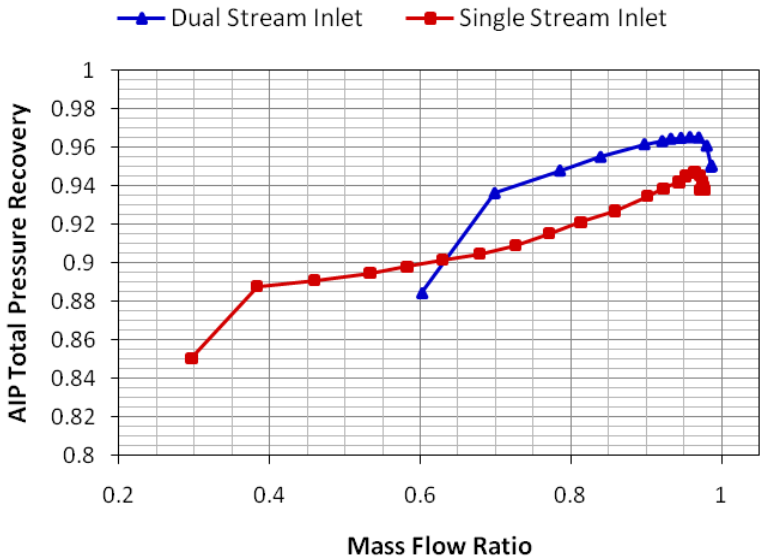

Figure 8. Cane curve comparison for the dual stream and single stream inlet configurations at Mach 1.7, 0˚ AOA.

On the low mass flow ratio end of the cane curve, the break in the slope indicates the point where the inlet goes into a buzz condition. The single stream inlet had a stable normal shock down to a mass flow ratio of 0.383, whereas the dual stream inlet was stable to 0.698. At the flight condition, the engine that the dual stream inlet was sized for operates over a nominal range of inlet capture mass flow ratios from about 0.85 to 1.0, so both inlets had more than adequate buzz margin to operate over the entire engine range.

Distortion was computed for the single stream and dual stream inlets using both DC60 and ARP 1420 distortion parameters. Distortion levels reported in this paper are the maximum value over the mass flow range, which occured at high mass flow ratios. At Mach 1.7, 0˚ AOA, the DC60 distortion level for the single stream inlet was 0.041, and the average DPCP was 0.031. For the dual stream inlet the DC60 distortion level was 0.037, and the average DPCP was 0.025.

While the dual stream and single stream inlets had different levels of performance and stability, their responses to the effects of Mach number, angle of attack and the vortex generators were similar due to the consistent geometries. More details on the single stream inlet can be found in Vyas et al[17]. The remainder of the results discussed here are for the dual stream inlet unless indicated otherwise.

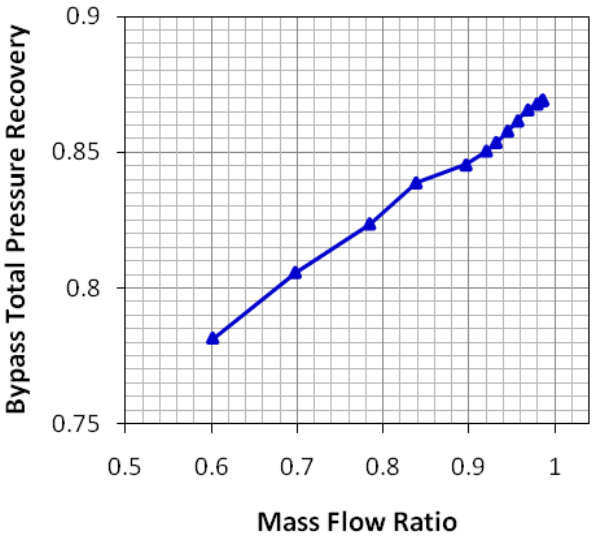

Figure 9. Bypass stream recovery over the range of mass flow ratios at Mach 1.7, 0˚ AOA.

B. Dual Stream Inlet Characteristics

The cane curve for the dual stream inlet at Mach 1.7, 0˚ AOA is shown again in Fig. 10 with schlieren images inset for every other data point. At the highest mass flow ratio, the normal shock is barely visible in the image because the shock is very close to the cowl lip. As the mass flow ratio decreases and the shock moves away from the cowl lip, specifically for the insets at mass flow ratios of 0.92 and 0.84, the curvature of the normal shock due to the relaxed compression is evident. The normal shock was very stable operating at low mass flow ratios until the inlet went into buzz. Near peak recovery, small amplitude low frequency unsteadiness was observed in the schlieren and AIP Kulites[15].

Figure 11 shows the inlet top dead center line static pressure profiles on the cowl and centerbody normalized by the freestream total pressure at Mach 1.7, 0˚ AOA, and a mass flow ratio of 0.969 which corresponds to peak core recovery. The inflection in the centerbody static pressure profile observed from 13 in to 21 in was due to primary struts. The static pressure profiles on the centerbody and cowl suggest a constant static pressure across the diffuser downstream of the primary struts. The normal shock was located at approximately x = 8.75 in on the centerbody. The static pressure ratio of 0.361 gives an isentropic Mach number of 1.3 ahead of the shock on the centerbody. At

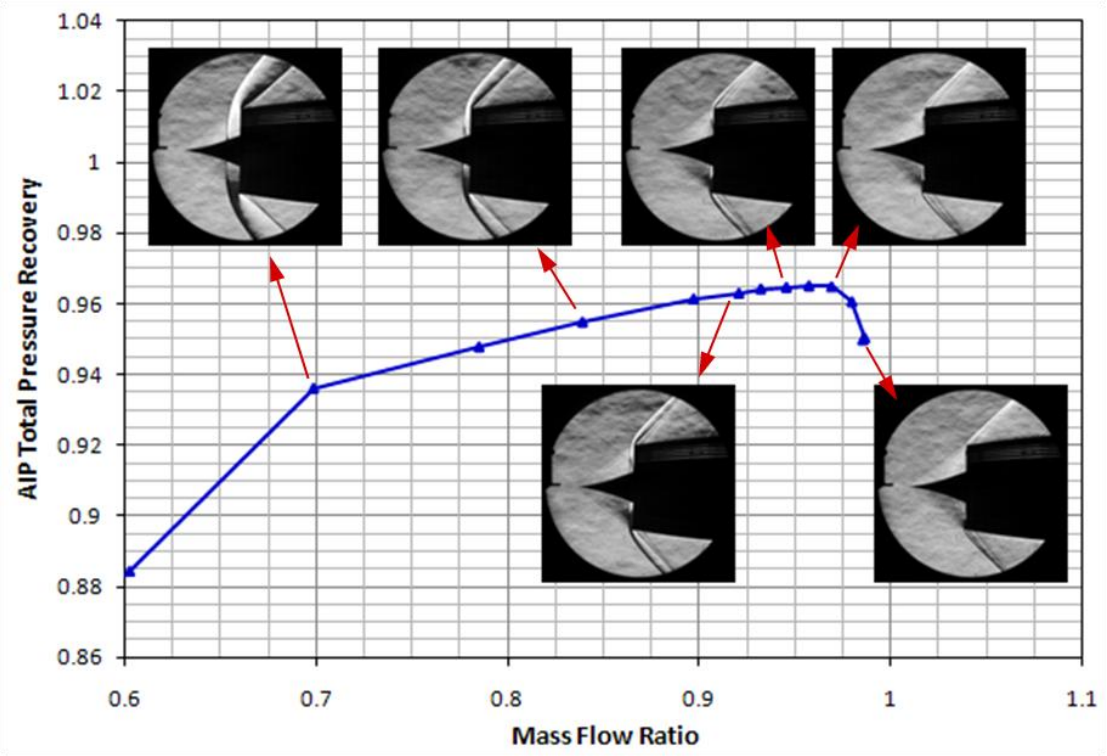

Figure 10. Dual stream inlet cane curve with schlieren images at selected points.

the AIP, taking into account a total pressure recovery of 0.965 gives a local static to total ratio of 0.771, which corresponds to an average AIP Mach number of 0.62.

CFD showed hysteresis in early designs of this inlet. To check for hysteresis during the test, two mass flow plug sweeps were completed at Mach 1.7, 0° AOA, shown in Fig. 12. The first was generated by progressively closing the mass flow plug to decrease the mass flow ratio resulting in the blue curve, which is the way we usually collected data during testing. The red curve was constructed in the opposite direction: starting with the mass flow plug nearly closed at a low mass flow ratio and working toward higher mass flow ratios. No hysteresis was evident.

Figure 13 shows cane curves for the dual stream inlet at 0° AOA for all of the Mach numbers tested. At Mach 1.8, the inlet reached a maximum mass flow ratio of 1.0. Decreasing Mach number decreases the maximum mass flow ratio achieved and increases the total pressure recovery. At the only subsonic point tested, Mach 0.5, the recovery is high over the entire mass flow range.

Whereas the single stream inlet is axisymmetric, the bypass geometry creates a top-to-bottom asymmetry in the dual stream inlet. Despite this, the cane curves for Mach 1.7 at varying angles of attack shown in Fig. 14 demonstrate little difference in overall inlet performance when comparing positive and negative angles of attack.

Increasing AOA decreased the maximum mass flow ratio because of spillage on the leeward side. At 1° AOA there was no change in the buzz margin compared to 0˚ AOA, but the maximum mass flow ratio decreased from 0.986 to 0.981 with an increase in DC60 distortion from 0.037 to 0.044. At 5° AOA the maximum mass flow ratio was 0.967 with a DC60 distortion level of 0.053. Across all angles of attack tested there was no measurable change in peak total pressure recovery. Increasing the AOA beyond 1° decreased the buzz margin.

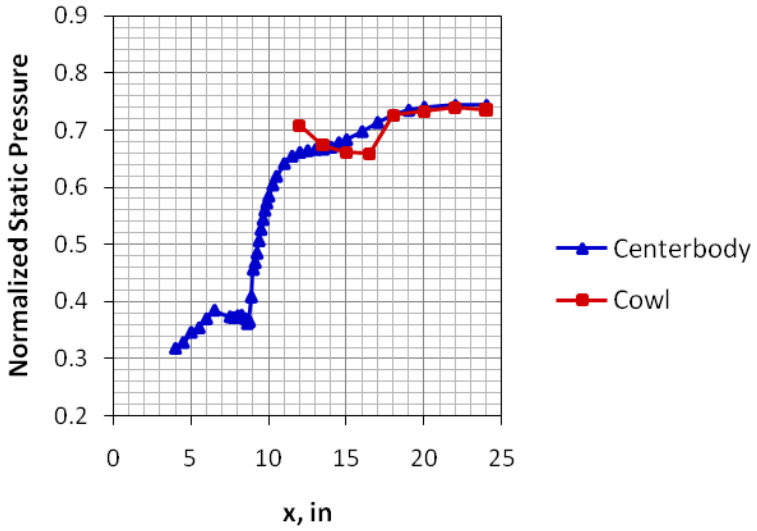

Figure 12. Static pressure profiles at Mach 1.7, 0° AOA, 0.969 mass flow ratio.

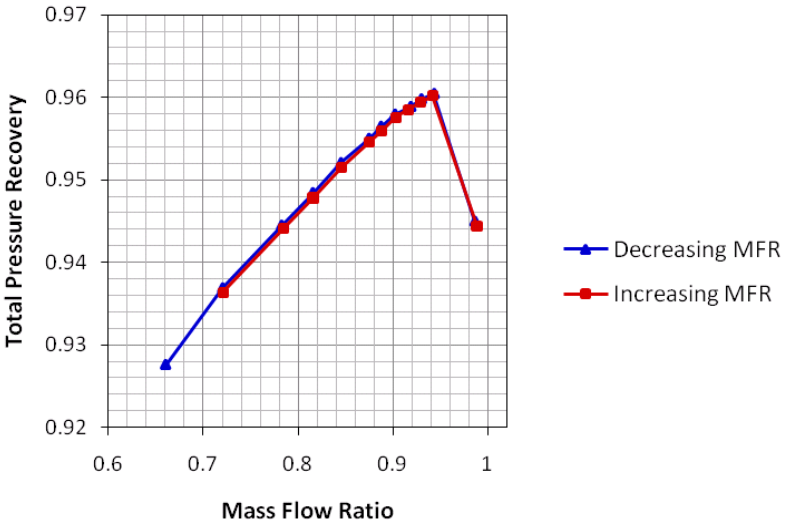

Figure 11. Consecutive cane curves testing for hysteresis effects.

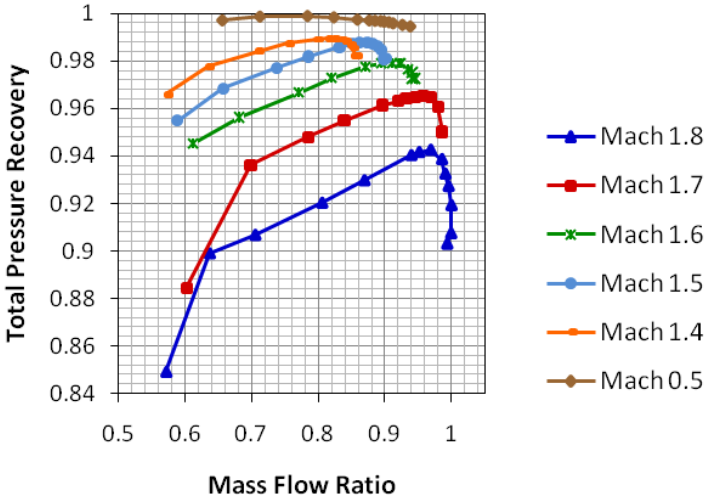

Figure 13. Cane curves for the dual stream inlet at 0˚ AOA.

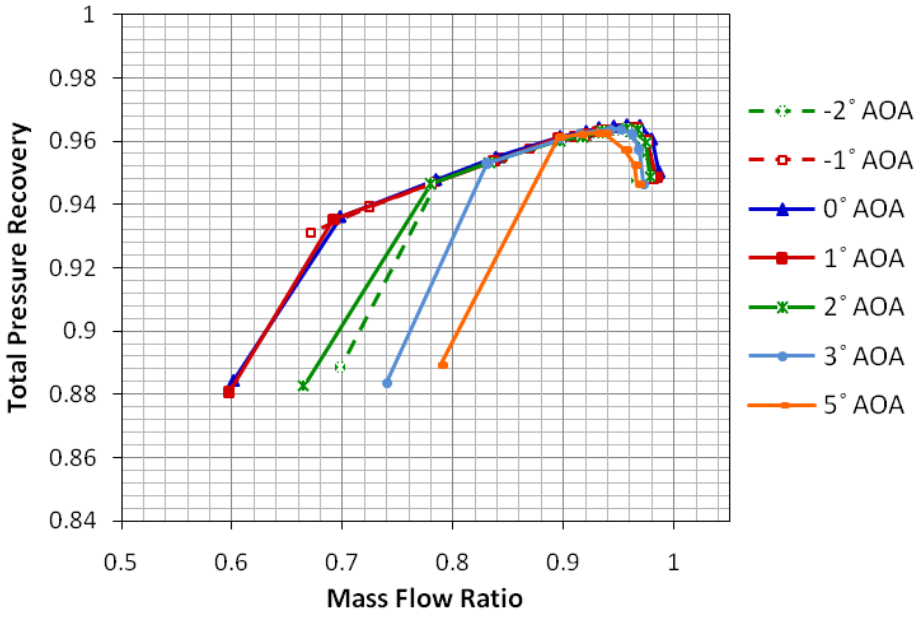

Figure 14. Cane curves for the dual stream inlet at Mach 1.7.

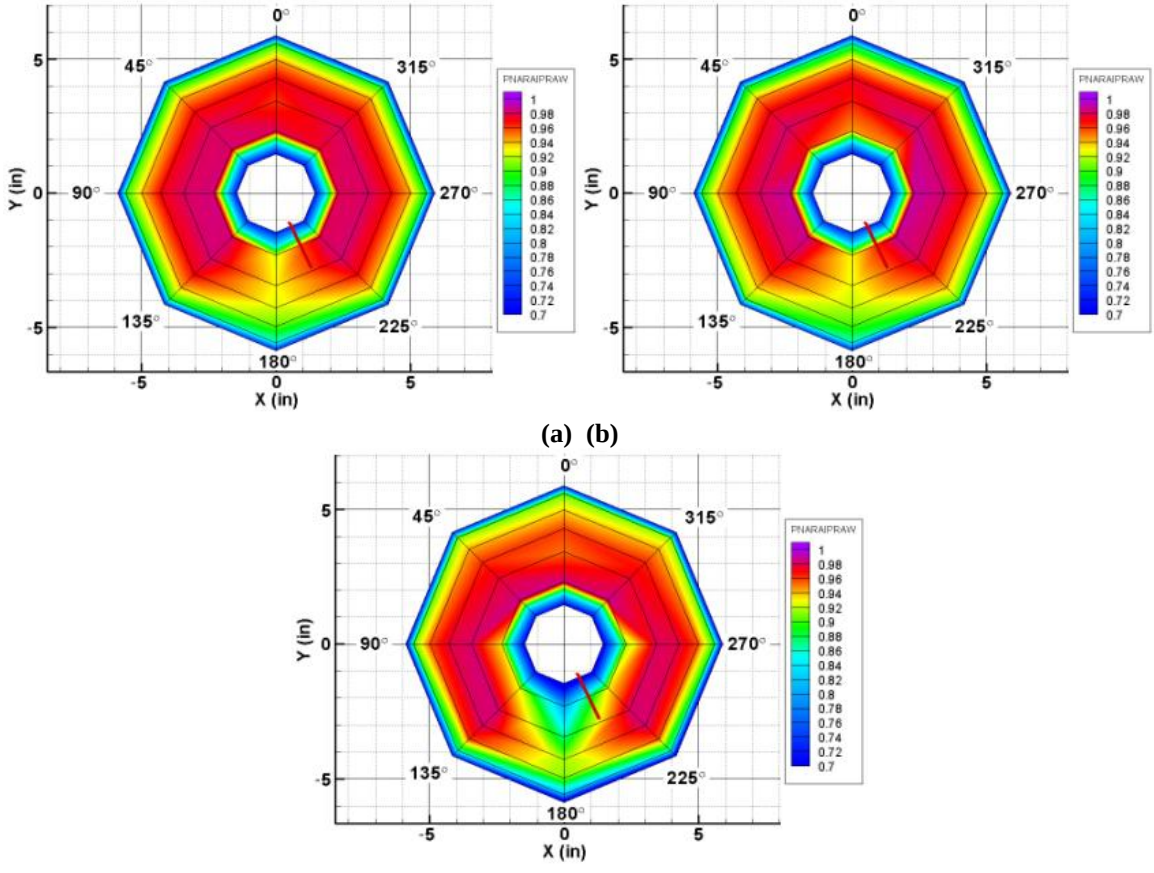

(a) (b)

(c)

Figure 15. AIP total pressure recovery contours shown for (a) 0° AOA, (b) -2° AOA, and (c) 5° AOA. View looking downstream.

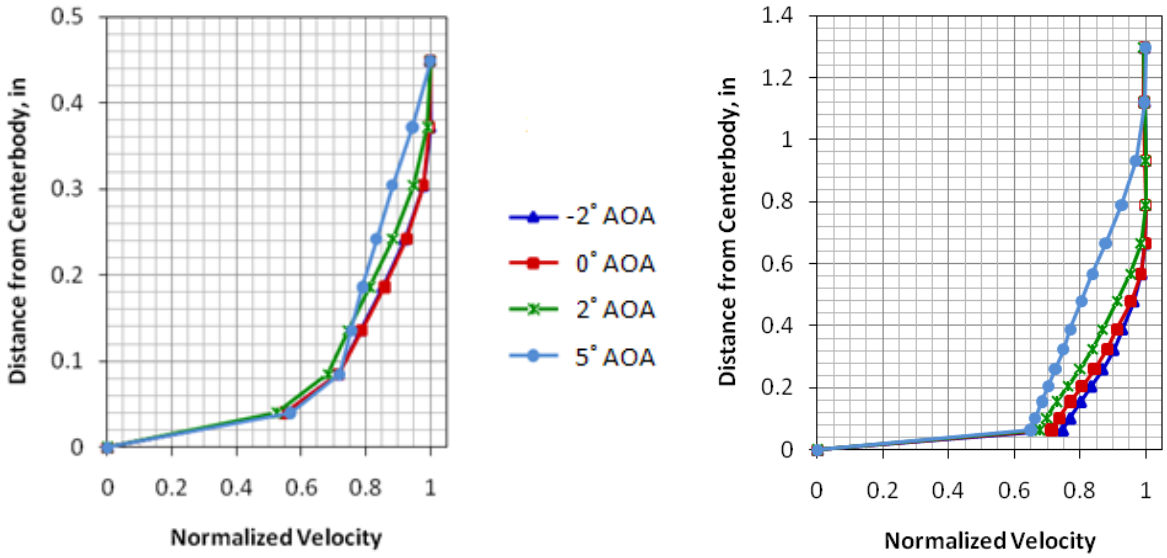

(a) **(b)**

Figure 16. Normalized boundary layer velocity profiles at the (a) upstream and (b) downstream boundary layer rakes for a mass flow ratio of approximately 0.965.

Figure 15 shows the AIP total pressure recovery contours at 0°, -2°, and +5° AOA. The rake at the 180° circumferential position is in the wake of one of the primary struts, and the associated loss in total pressure can be seen. In the -2° AOA contour, a slight decrease in the total pressure recovery on the top side of the centerbody can be seen. For the 5 degree case, the total pressure deficit is on the bottom side of the centerbody and influences can also be seen in the 90° and 270° rakes. The red line extending from the centerbody at 202.5° in Fig. 15 indicates the circumferential location of the downstream boundary layer rake.

The boundary layer velocity profiles at the upstream and downstream boundary layer rakes are shown in Fig. 16. Both rakes are on the bottom side of the inlet. At positive angles of attack both rakes show decreases in the boundary layer fullness consistent with the low pressure region seen in the contour. At -2° AOA no change in the profile is seen at the upstream rake, but the boundary layer is fuller in the downstream rake.

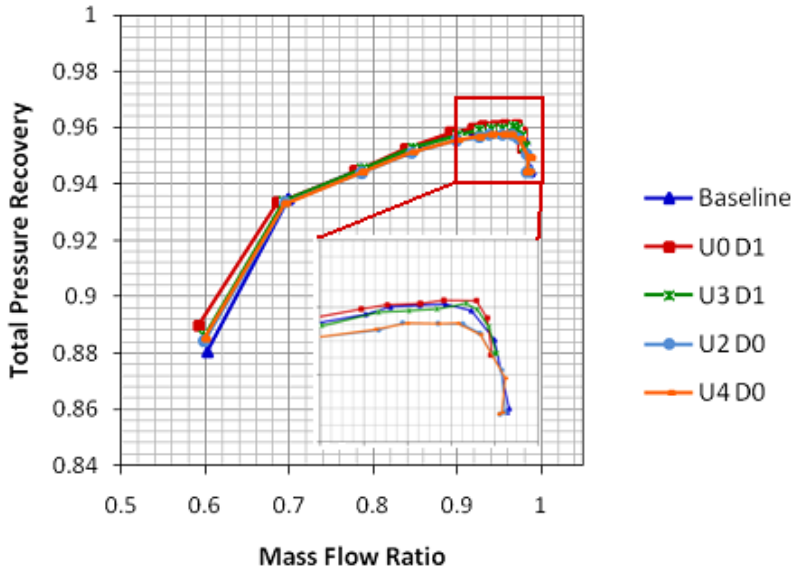

Figure 17. Comparison of cane curves for the dual stream inlet at Mach 1.7, 0˚ AOA for each of the VG configurations tested.

C. Vortex Generator Effects

Figure 17 shows cane curve comparisons for the VG configurations tested on the dual stream inlet at Mach 1.7, 0° AOA. The configurations with only upstream VGs (U2D0 and U4D0) caused a reduction in peak recovery of about 0.005. Both cases that included the large downstream vanes (U0D1 and U3D1) had no impact on the measured total pressure recovery. There was no measurable change in maximum recorded mass flow ratio for any of the cases.

The upstream boundary layer rake velocity profiles for the VG configurations are shown in Fig. 18 at Mach 1.7, 0° AOA, for the peak total pressure recovery. The forward boundary layer rake is halfway between the primary struts. The cases

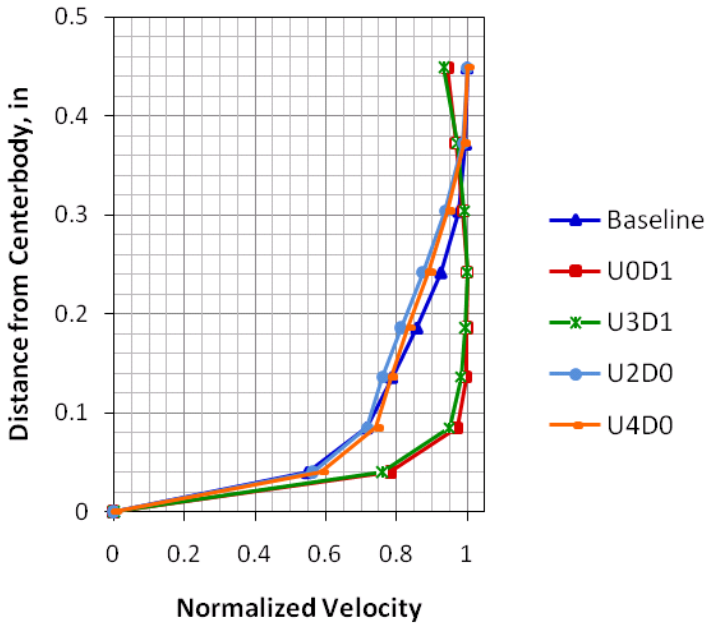

Figure 18. Forward boundary layer rake velocity profiles for the VG configurations.

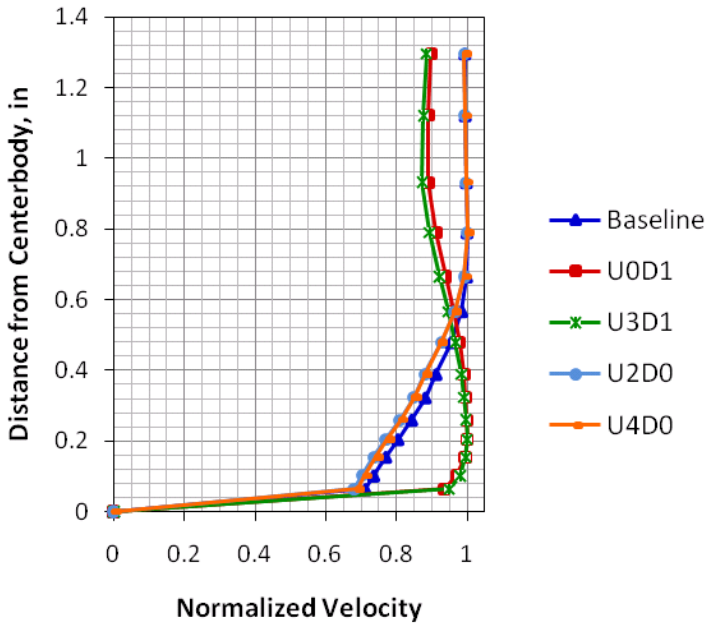

Figure 19. Aft boundary layer rake velocity profiles for the VG configurations.

U0D1 and U3D1 show significantly fuller profiles because the rake is in the upwash produced by the large D1 vanes. The addition of the upstream U3 split ramp VGs slightly decreases the velocities throughout the profile. For the cases with only upstream VGs, the mixing caused by the small devices can be seen in the profiles as a slight increase in velocity near the wall and a velocity deficit in the outer boundary layer.

Similar comparisons can be made for the downstream boundary layer rake velocity profiles shown in Fig. 19. The aft boundary layer rake is in line with one of the vanes. Trends are similar to the upstream rake except that the differences due to the addition of the upstream split ramps between U0D1 and U3D1 are not noticeable near the wall. At this circumferential location the U2D0 and U4D0 cases cause a slight velocity deficit throughout the boundary layer.

In terms of distortion, the large vanes of the D1 VG configuration decreased the DC60 distortion slightly from 0.037 to 0.033 at Mach 1.7, 0° AOA. At 5° AOA the distortion was decreased from 0.053 for the baseline case to 0.035 with the D1 vanes. The upstream devices had no measurable impact on distortion, with or without downstream VGs.

D. Inlet Buzz Cycle

High speed schlieren of the single stream inlet captured during the buzz cycle provided a detailed view of the flow conditions during inlet buzz. Figure 20 shows the axial location of the normal shock normalized by the spike tip to cowl lip distance during one representative buzz cycle at Mach 1.7, 0° AOA. In the figure, a normalized value of 0 corresponds to the cowl lip, and a normalized value of 1 corresponds to the spike tip. The total time for the cycle shown was 0.045 seconds, which gives a buzz frequency of approximately 22 Hz.

Shock positions were manually determined from the schlieren images for 40 images at equal time intervals during the cycle. Observations from other cycles in this and other buzz sequences show that this cycle is representative; however, results shown represent only a single period.

The buzz cycle consisted of four phases: shock travelling upstream, shock dwelling at the tip, shock travelling downstream, and shock dwelling near the cowl. The four phases were not of equal duration during the cycle. The shock travelled upstream during 22% of the cycle, dwelled at the spike tip for 34% of the cycle, travelled downstream over 31% of the cycle, and dwelled near the cowl for only 13% of the cycle.

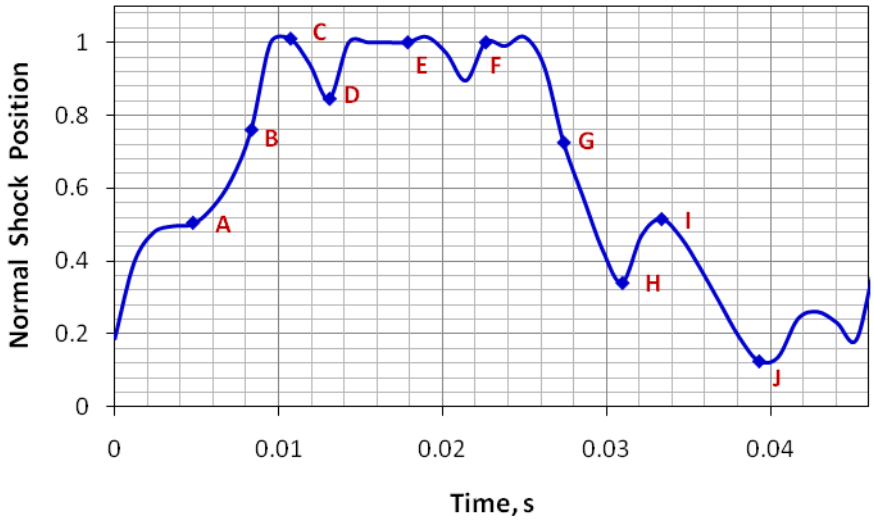

Figure 20. Time trace of normal shock position during a buzz cycle.

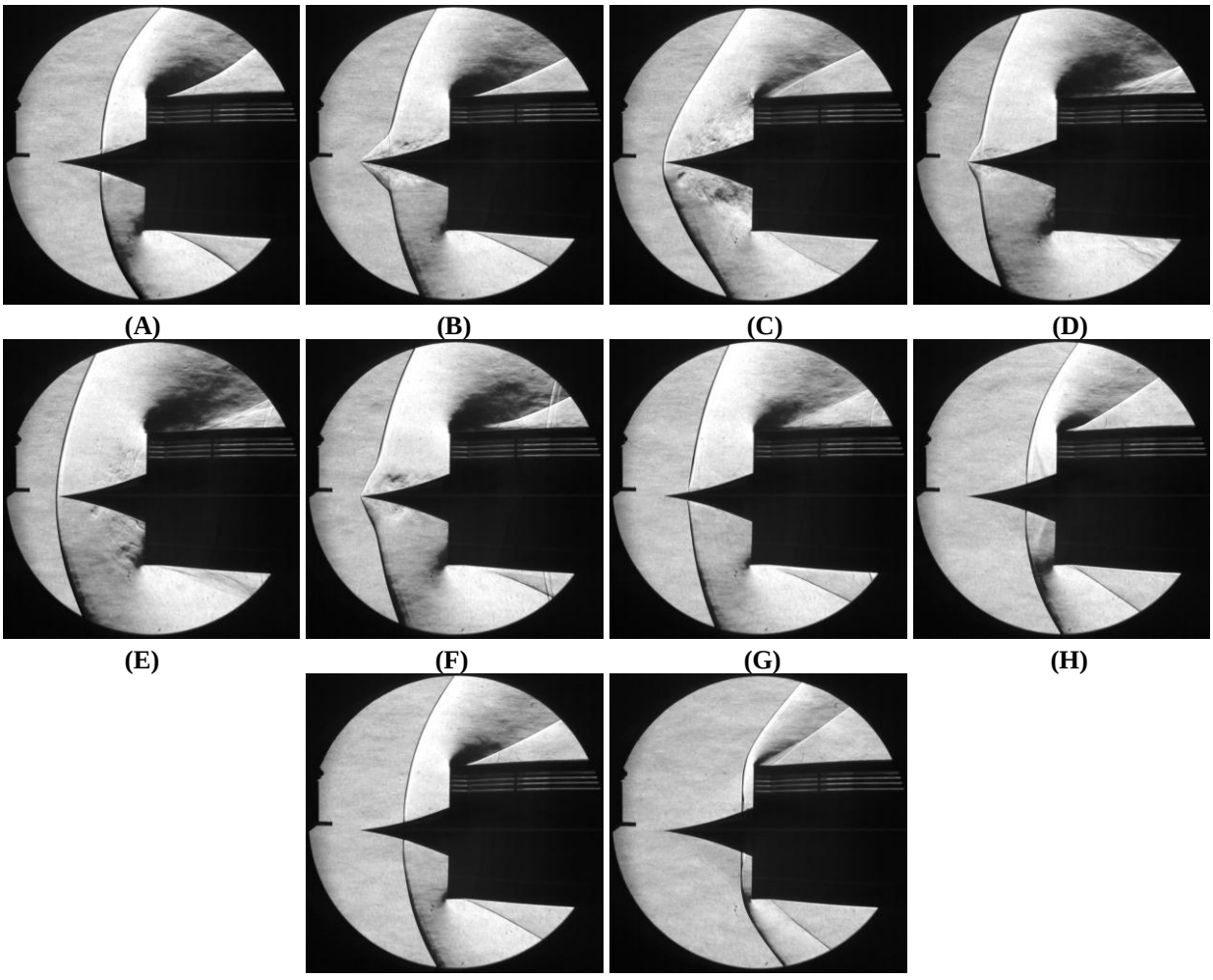

Figure 21. Schlieren images of the single stream inlet during a buzz cycle. Times correspond to the matching labels in Fig. 19.

Images of the shock structure during the buzz cycle are shown in Fig. 21 with labels, A through J, that correspond to the markers in Fig. 20. Images A and B show the shock travelling upstream. In image A, a small separation had developed at the foot of the normal shock. Images C through F show typical images while the shock was dwelling at the spike tip. The normal shock exhibited a higher frequency pulsing during this phase of the cycle. In figure F vortices are visible about a third of the distance from the spike tip to the cowl lip. Sometimes these vortices were ingested by the inlet and other times they were diverted around the cowl lip.

The phase of the buzz cycle with the shock travelling downstream is represented in images G through I. In image H a wave is visible downstream of the normal shock. The high frame-rate schlieren shows that this wave propagated upstream inside the inlet and pushed the normal shock upstream, as seen in image I. During the buzz cycle the shock was not pulled all the way to the cowl lip. The most downstream normal shock position seen for this buzz cycle is shown in image J.

E. Surface Flow Visualization

To help understand the effects of the VGs on the internal flowfield surface flow visualization images, both oil flow and pressure sensitive paint (PSP), were recorded. The image in Fig. 22 is a composite of the PSP contours and the surface streaks from the oil flow. The low pressure regions are visible in blue on the aft surfaces of the ramp and on the centerbody at the foot of the ramp. The wake from the device is clearly visible in the oil flow. One notable difference from prior oil flow studies done for flat wall geometries is the curvature of the oil flow lines around the device due to the contour of the centerbody. Additionally, the surface flow visualization results showed a separation region just downstream of the normal shock for large mass-flow ratios. This separation is likely responsible for the normal shock unsteadiness noted at high mass flow ratios; however the unsteadiness was not a concern due to the small amplitude of the disturbance. Quantitative results of the surface flow visualization are presented in Herges et al[18].

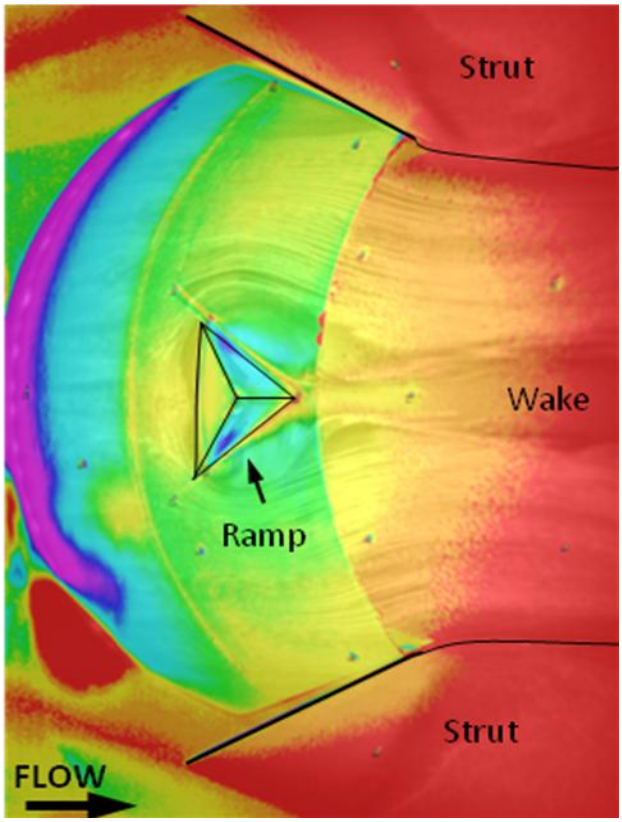

Figure 22. Pressure sensitive paint overlaid on oil flow contours on the internal centerbody surfaces.

IV. Conclusion

During the course of the test, the low-boom inlet concept was demonstrated to have high recovery, excellent buzz margin, and high operability. The dual stream inlet generated high AIP recovery because the bypass channel diverted the high loss flow near the cowl around the engine. Both the single stream and dual stream inlets had sufficient buzz margin to operate over a representative range of engine operation. While the dual stream and single stream inlets had different levels of performance and stability, their response to the effects of Mach number, angle of attack and the vortex generators was similar due to the consistent geometries.

For the dual stream inlet, it was shown that on-design near-zero spillage can be achieved for a simple, fixed-geometry relaxed external compression inlet system featuring high inlet-bypass flow. Massive amounts of secondary bypass flow were fully and predictably controlled in a stable manner across a wide Mach, flow, and angle of attack operational space. Excellent core stream performance was maintained across the supersonic speed range, even at high angle of attack, when relaxed compression and high-bypass geometry were combined.

The vortex generators had very little effect on overall inlet performance, but the downstream vortex generators decreased distortion, especially at angle of attack. The upstream vortex generators were designed to control any normal shock instabilities or separation of the boundary layer due to the large shoulder turning angle. The baseline inlets without any flow control performed better than expected in this regard, so these devices proved unnecessary

for this inlet configuration. The upstream devices caused a slight decrease in total pressure recovery, and had no measurable impact on distortion.

Additional observations:

- Computational fluid dynamics solutions were used effectively during the design process to aid in test planning , and this use increased confidence in the use of modeling and simulation tools to design inlets of this class with flow control.
- The normal shock was very stable operating at mid to low mass flow ratios until the buzz point occurred. Near peak recovery, small amplitude low frequency unsteadiness was observed in the schlieren and AIP kulites.
- Aerodynamic performance, pressure sensitive paint, high speed schlieren and oil flow visualization data were collected during the testing, which showed a separation region just downstream of the normal shock for large mass-flow ratios.

Acknowledgments

The authors would like to acknowledge the support of the team that made this work possible: specifically, researchers at the University of Illinois Urbana-Champaign, University of Virginia, and Gulfstream Aerospace Corporation, the model design and fabrication work by TriModels, Inc., and the facility team at the 8- x 6-foot supersonic wind tunnel at NASA GRC. The Supersonics Project of the NASA Fundamental Aeronautics Program supported this work.

References

[1]Conners, T.R., Gulfstream Aerospace Corporation, Savannah, GA, U.S. Patent Application for "Low Shock Strength Propulsion System," Application No. 12/257,982; Filed 24 Oct. 2008.

[2]Conners, T.R., Howe, D.C., and Henne, P.A., Gulfstream Aerospace Corporation, Savannah, GA, U.S. Patent Application for "Isentropic Compression Inlet for Supersonic Aircraft," Application No. 11/639,339; Filed 15 Dec. 2006.

[3]Conners, T.R. and Howe, D.C., "Supersonic Inlet Shaping for Dramatic Reductions in Drag and Sonic Boom Strength," AIAA-2006-0030, January 2006.

[4]Conners, T. R. and Wayman, T. R., "The Feasibility of High-Flow Nacelle Bypass for Low Sonic Boom Propulsion System Design," AIAA 29th Applied Aerodynamics Conference, June 27-30, 2011 (to be published.)

[5]Conners, T. R., Merret, J. M., Howe, D. C., Tacina, K. M., and Hirt, S. M., "Wind Tunnel Testing of an Axisymmetric Isentropic Relaxed External Compression Inlet at Mach 1.97 Design Speed," AIAA paper 2007-5066, July 2007.

[6]Conners, T.R., Gulfstream Aerospace Corporation, Savannah, GA, U.S. Patent Application for "Low Shock Strength Inlet," Application No. 12/000,066; Filed 7 Dec. 2007.

[7]Tacina, K.M., Hirt, S.M., Conners, T.R., Merret, J.M., and Howe, D.C., "Dynamic Analysis of Wind Tunnel Data from an Isentropic Relaxed Compression Inlet," AIAA paper 2007-5073, July 2007.

[8]Soeder, R.H., "NASA Lewis 8- By 6-Foot Supersonic Wind Tunnel User Manual," NASA-TM-105771, 1993.

[9]Society of Automotive Engineers, Inc., "Gas Turbine Engine Inlet Flow Distortion Guidelines," ARP1420 Rev B, 2002.

[10]Conners, T.R., and Howe, D.C., "Supersonic Inlet Shaping for Dramatic Reductions in Drag and Sonic Boom Strength," AIAA Paper 2006-30, Jan. 2006.

[11]Chima, R. V., Hirt, S. H., and Reger, R., "Axisymmetric Calculations of a Low-Boom Inlet in a Supersonic Wind Tunnel, " AIAA 29th Applied Aerodynamics Meeting, June 27-30, 2011 (to be published.)

[12]Chima, R.V., Conners, T.R., and Wayman, T.R., "Coupled Analysis of an Inlet and Fan for a Quiet Supersonic Jet," AIAA Paper 2010-479, Jan. 2010. Also NASA TM-2010-216350.

[13]Chima, R. V., "Computational Analysis of a Low-Boom Supersonic Inlet," AIAA 29th Applied Aerodynamics Conference, June 27-30, 2011 (to be published.)

[14]Gillen, T., and Loth, E., "Vortex Generators for a Dual-Stream Low-Boom Inlet," AIAA 29th Applied Aerodynamics Conference, June 27-30, 2011 (to be published.)

[15]Rybalko, M., Loth, E., Chima, R. V., Hirt, S. M., and DeBonis, J. R., "Micro Ramps for External Compression Low-Boom Inlets," AIAA Paper 2009-4206, June 2009.

[16]Rybalko, M., and Loth, E., "Vortex Generators for a Single-Stream Low-Boom Inlet," AIAA 29th Applied Aerodynamics Conference, June 27-30, 2011 (to be published.)

[17]Vyas, M. and Wayman, T. R., "Experimental Investigation of Micro Vortex Generators on a Low-Boom Supersonic Inlet," AIAA 29th Applied Aerodynamics Conference, June 27-30, 2011 (to be published.)

[18]Herges, T., "Surface Flow and PSP Measurements in the Large-Scale Low-Boom Inlet," AIAA 29th Applied Aerodynamics Conference, June 27-30, 2011 (to be published.)